REPORT DOCUMENTATION PAGE

AFRL-SR-AR-TR-03-

0323

1. REPORT DATE (DD-MM-YYYY) 25-06-2003	2. REPORT TYPE Final Report	3. DATES COVERED (From - To) September 2003 – June 2003

4. TITLE AND SUBTITLE

Time-Exposure Acoustics for Imaging Underground Structures

5a. CONTRACT NUMBER
F49620-02-C-0096

5b. GRANT NUMBER

5c. PROGRAM ELEMENT NUMBER

6. AUTHOR(S)

I.J. Won, Alan Witten, and Steve Norton

5d. PROJECT NUMBER

5e. TASK NUMBER

5f. WORK UNIT NUMBER

7. PERFORMING ORGANIZATION NAME(S) AND ADDRESS(ES)

Prime Contractor
Geophex, Ltd.
605 Mercury St.
Raleigh, NC 27603

Subcontractor
University of Oklahoma
School of Geophysics
Norman, OK73019

8. PERFORMING ORGANIZATION REPORT NUMBER

Geophex #1199

9. SPONSORING / MONITORING AGENCY NAME(S) AND ADDRESS(ES)

AF Office of Scientific
4015 Wilson Blvd, Room 713
Arlington, VA 22203
Attn: Dr. Jon Sjogren

10. SPONSOR/MONITOR'S ACRONYM(S)
AFOSR/NM

11. SPONSOR/MONITOR'S REPORT NUMBER(S)

12. DISTRIBUTION / AVAILABILITY STATEMENT

Approved for public release, distribution unlimited

20031028 148

13. SUPPLEMENTARY NOTES

14. ABSTRACT

We have developed a new technique for imaging underground facilities based on the passive monitoring of acoustic emissions from both stationary and moving equipment within such facilities. It is well know that all mechanical devices, such as motors, gears, etc, emit acoustic signals. It is possible to identify an acoustic source based on its noise spectrum.

Passive "listening" has been considered and employed in the past to detect underground structures based upon noise emitted from within. The fundamental difference in our approach is that we rigorously considered the inverse source problem subject only to the assumption that the noise source is localized. Rather than using time delays across a sensor array to "triangulate" on the source, our method, known as time-exposure acoustics (TEA), coherently sums the data receiver over an array of sensors and back-propagates it into the host geologic formation. This procedure yields an image of the source that is similar to the image formation process used in reflection seismic exploration.

15. SUBJECT TERMS

16. SECURITY CLASSIFICATION OF: Unclassified			17. LIMITATION OF ABSTRACT	18. NUMBER OF PAGES	19a. NAME OF RESPONSIBLE PERSON Dr. I.J. Won
a. REPORT	b. ABSTRACT	c. THIS PAGE		8 plus Appendices	19b. TELEPHONE NUMBER (include area code) (919) 839-8515

Standard Form 298 (Rev. 8-98)
Prescribed by ANSI Std. Z39.18

Final Report: Item 0001AD
Phase I STTR Contract F49620-02-C-0096:
Time-Exposure Acoustics for Imaging Underground Structures

from
Geophex, Ltd. and University of Oklahoma

Submitted to
Dr. Jon Sjogren, Program Manager
AFOSR/NM
4015 Wilson Blvd, Room 713
Arlington, VA 22203

1. General Project Information

AFOSR awarded Geophex this Phase I STTR contract effective September 1, 2002. It requires three Status Reports and a Final Report as follows:

Item	Report	Performance Period	Due Date
0001AA	Status Report 1	Sep 1, 02 – Oct 31, 02	Nov 15, 2002
0001AB	Status Report 2	Nov 1, 02 – Jan 31, 03	Feb 17, 2003
0001AC	Status Report 3	Feb 1, 03 – Apr 30, 03	May 15, 2003
0001AD	Final Report	Sep 1, 02 – Aug 31, 03	Sep 30, 2003

The following personnel are involved in this project:

Name	Function	Specialty	Employer
Dr. Steve Norton	Co-PI	Geophysicist	Geophex
Dr. I.J. Won	Co-PI	Geophysicist	Geophex
Dr. Alan Witten	Academic PI	Geophysicist	University of Oklahoma
Mr. Alex Oren	Staff	Electrical Engineer	Geophex
Mr. Frank Funak	Staff	Programmer	Geophex

2. Background

Underground facilities (UGF) may be detected and monitored by either active or passive methods. Active methods introduce some form of energy into the ground, typically mechanical or electromagnetic waves. UGF will be manifested in this data since they are air-filled and, as such, present a substantial change in mechanical or electrical properties. A 3-D image can be reconstructed from this data that shows the location and extent of a UGF (Witten, Won, and Norton, 1997 a and b; Witten, Schatzberg, and Devaney, 1996; Witten, 1991; Witten, Levy, Ursic, and White, 1995).

In spite of the success of these methods, the active methods do have restrictions that limit their applicability. First, the deployment of active sources, in many situations, may not be possible. Furthermore, the methods require that sources and receivers be distributed over some regular

grid system. Such requirements may be impossible to satisfy, particularly if sensors must be dropped from aircraft. There will always be a loss of signal with distance from the source so that active systems employing both sources and receivers on the ground surface must travel a distance that is, at a minimum, twice the target depth. This attenuation will always limit the depth to which active systems can be applied.

Passive methods detect and characterize UGF from sources generated by the facility itself. When a UGF is quiescent, it cannot be detected by a passive method. However, when active, it can be detected by remotely monitoring emissions. Applying specific signal processing techniques allows the source to be localized and characterized by its emitted spectrum. These techniques do not require dense or uniform sensor spacing. Since the energy must only travel one way, upward from the source to the detectors, it is far less limited than active methods.

In time-exposure photography, low intensity light is integrated over time to enhance image brightness in poor lighting conditions. A similar concept is possible in acoustics, known as Time-Exposure Acoustics (TEA: Norton and Won, 2000: attached here as Appendix B), wherein acoustic images are reconstructed from passively acquired seismic noise, such as that generated inside a UGF. Noise sources include motor-driven machinery (generators, ventilation fans, etc.) and moving vehicles in the UGF or through tunnels that may be a part of its infrastructure. Figure 1 illustrates the creation of a wave front impinging on a surface geophone array due to a moving vehicle inside a tunnel. The data are recorded by a geophone array on the surface and processed on site in real time. The imaging of subsurface sources using passive seismic data is potentially attractive for several reasons:
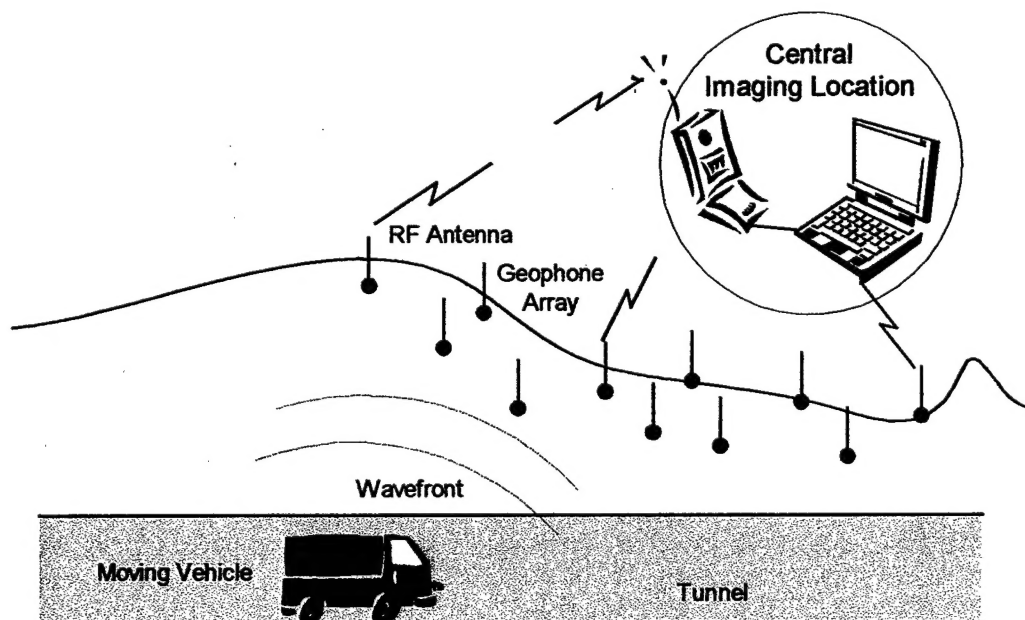

Figure 1: Wavefront impinging on a geophone array generated by subsurface vehicle.

- The TEA allows a long time exposure that accumulates faint sources, progressively improves the resolution, and displays the current image in real time.

- The signal is integrated over time whenever the source is "on," creating an image that shows collective and historic activities. In this way, weak sources should eventually reveal themselves after a sufficient exposure. For a moving source, such as a vehicle moving in a tunnel, the time exposure will trace the path of the vehicle.

- Passive seismic data can be acquired more discretely than active-source data, particularly in a hostile environment or when the use of active sources is tactically impractical.

- Since the image is constructed in real time, there is no need of bulky data storage.

3. Simulation Studies

Appendix A describes the TEA algorithm originally developed by Geophex in 2000 (Norton and Won, 2000). We first apply the TEA algorithm to synthetic data in order to assess its efficacy and to identify conditions under which its performance could be degraded. The model includes an underground acoustic source and an array of receivers distributed on the ground surface directly above the source. The simulated sources have included impulsive points, incrementally moved impulsive points, and continuous random and periodic point sources.

In the first test, an impulsive point source is located somewhere in the subsurface and synthetic data is generated for a linear array of 64 receivers directly above this point (Fig. 2a). An arbitrary time shift is introduced (Fig. 2b) and the TEA algorithm is applied. Figure 2c presents a 2-D display of the likelihood of source location in false color with red corresponding to the highest computed values. The dark red node in this image occurs at the precise source location.

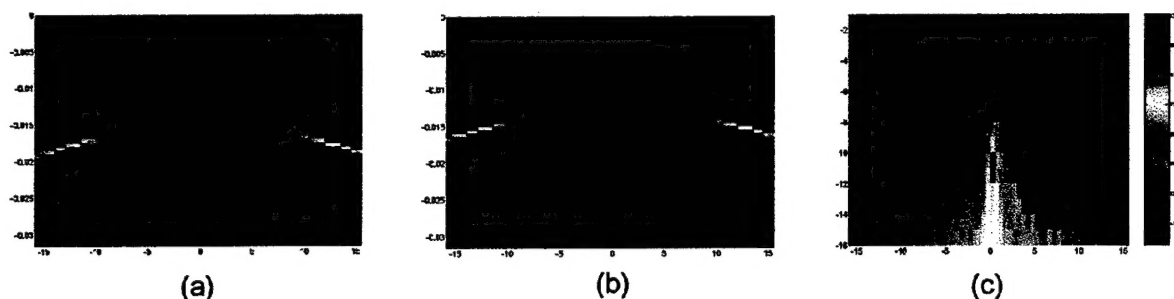(a)   (b)   (c)

Figure 2: (a) Synthetic data for an impulsive point source, (b) that has been shifted, and (c) the image resulting from the application of the TEA algorithm.

Figure 3a displays a random time-series and Fig. 3b shows the synthetic data acquired for a subsurface point source having this output. The TEA image is given in Fig. 3c displaying a result comparable to the impulsive point source (Fig. 2c).
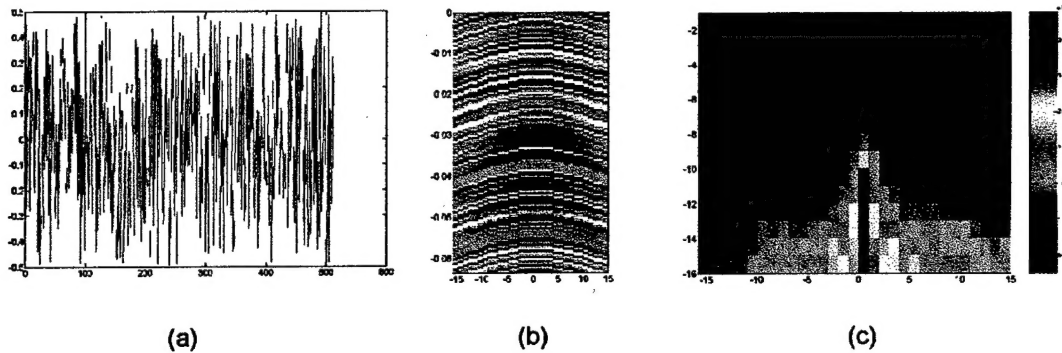
(a) (b) (c)

Figure 3: A random time series (a), the synthetic data resulting when these temporal variations are applied to a point source (b), and (c) the TEA image.

The final 2D example is for multiple impulsive point sources. In this simulation, five point sources are distributed over a uniform depth in the subsurface and each source is sequentially fired such that there is a time delay that increases with horizontal source location. The synthetic data is provided in Fig. 4a and the TEA image in Fig. 4b. If this reconstruction were perfected, five distinct highs should appear at uniform horizontal intervals and at the same depth. These features do appear in the image along with several weaker spurious responses. These artifacts are associated with locations in the data where there are high signal strengths associated with points of intersection of individual hyperbolas.
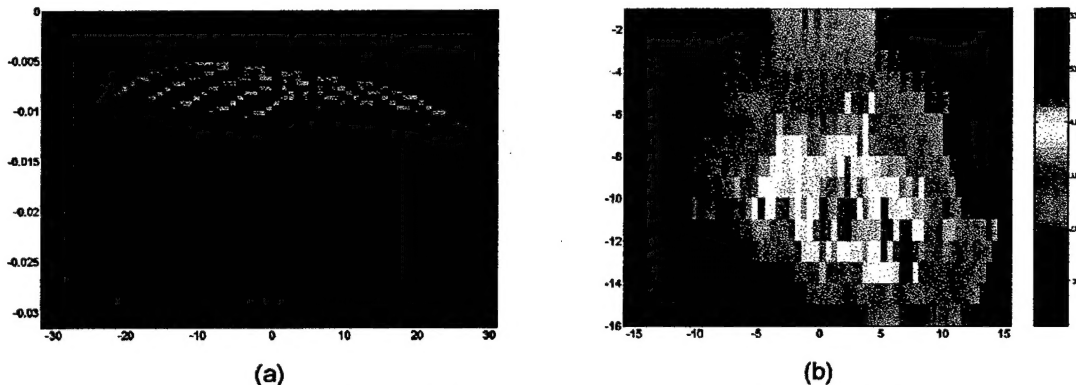

(a) (b)

Figure 4: Five sequentially fired impulsive point sources (a) and (b) the TEA image.

4. Confirmatory Field Tests

To confirm the TEA algorithm, we acquired field data over a small cave in limestone in southeastern Oklahoma. The data were acquired over a 30 by 35 ft planar and slightly sloping region over a short cave accessed through an open sinkhole (Fig. 5a). An array of 48, 40Hz geophones was distributed as an 8 by 6 array as shown in Fig. 5b.

An acoustic signal was created within the cave by gently tapping on the limestone surface of the cave. Source locations were randomly selected within the cave over about 25 ft of its accessible length. About ten blows were applied to each source position.

30 ft

● geophones

35 ft

5'

6'

10'

cave
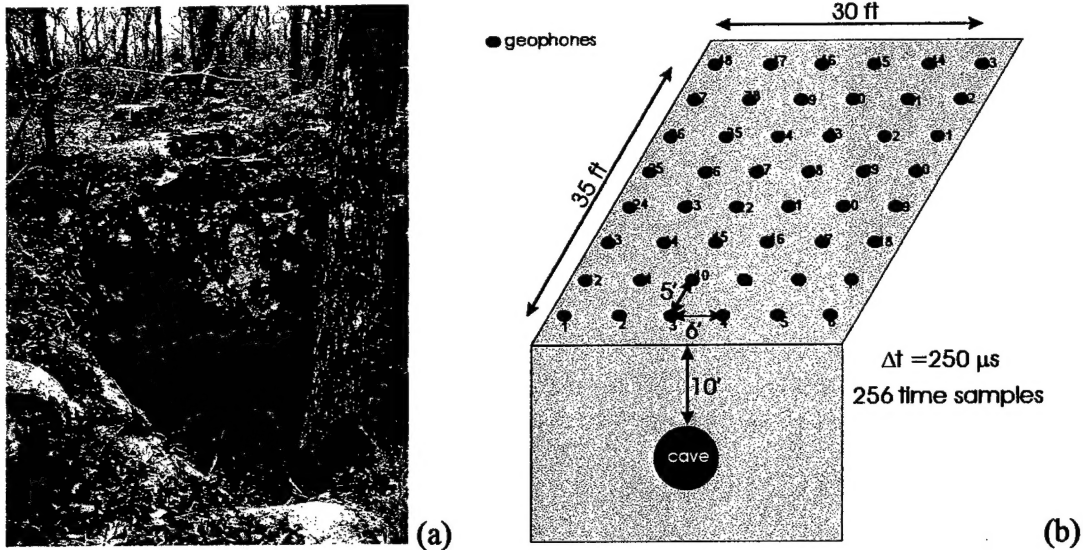
Δt =250 μs

256 time samples

(a)

(b)

Figure 5: (a) The sinkhole cave access in the foreground and orange pin flags at geophone positions in the background; (b) general geometry of the geophone layout relative to the cave.

5. TEA Applied to Field Data

Figure 6a presents data acquired from one particular hammer blow within the cave. The vertical axis is the time sample number and the horizontal coordinate is the receiver index as identified in Fig. 5b. A sequence of hyperbolas is evident in the data and these are from the lines of geophones closest to a point on the ground surface directly above the source. The result of the application of the TEA algorithm is given in Fig. 6b where the maximum computed source likelihood is displayed as a surface in 3-D enclosed in red. The location of the impulsive point source is well resolved.
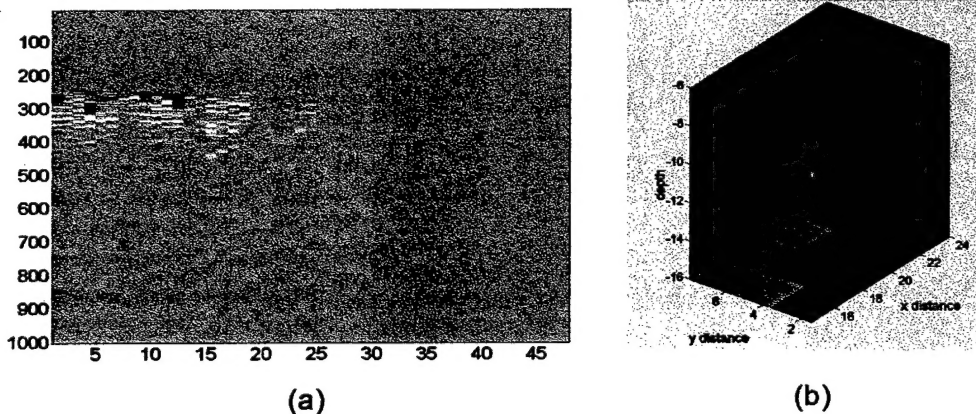

(a)

(b)

Figure 6: The data acquired above an impulsive point source located within a cave (a) and (b) the source location as provided by the TEA algorithm.

Figure 7 presents acquired data similar to that shown in Fig. 6 but for a different source location and here the character of the data is distinctly different. Most significant is the "ringing" that is absent in Fig. 6. This effect is believed to be caused by the excitation of resonant modes of the cave. The application of the TEA algorithm to an early time portion of this data set is provided in Fig. 8a and the entire cave is revealed from a single source point. Using the full data series, the result of the TEA algorithm (Fig. 8b) clearly shows that the resonance apparent in Fig. 8 is a result of the excitation of resonant modes of both the known cave and deeper unknown void.
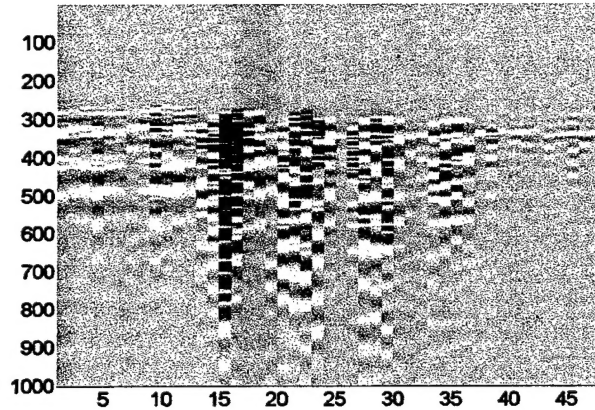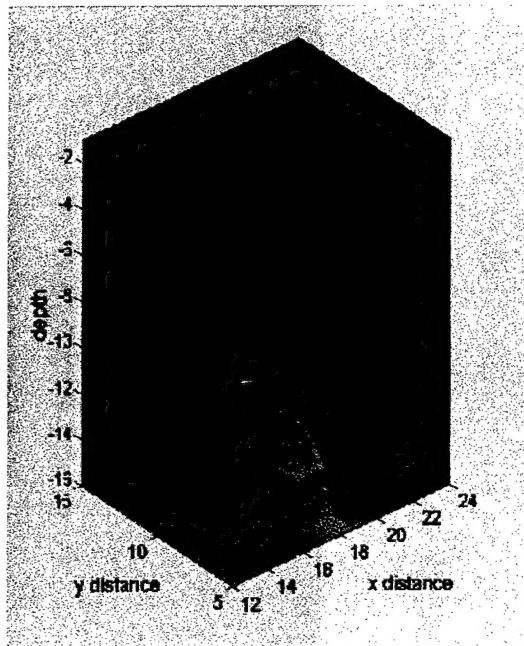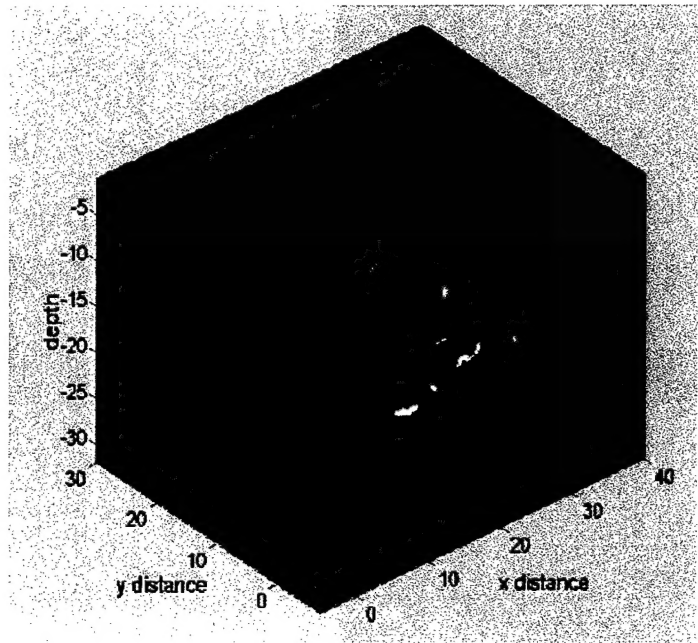

Figure 7: Data acquired from a source point located deep within the cave.

(a)   (b)

Figure 8: TEA images derived from the data given in Fig. 8 for (a) a time-windowed subset of the data and (b) the full data set. Note that the image indicates an additional bigger cave below the small known one.

6

6. Moving Source Field Studies

To demonstrate the TEA algorithm for a moving source, data were acquired on the Geophex property in Raleigh, NC. Specifically, two perpendicular lines of 24 geophones each were used and a moving source was created by striking the ground with a hammer at various locations. Figure 9 presents the source locations (circles) and the two geophone lines. Along each line, the geophone spacing was 5 ft. and temporal samples were acquired at 2 ms intervals.
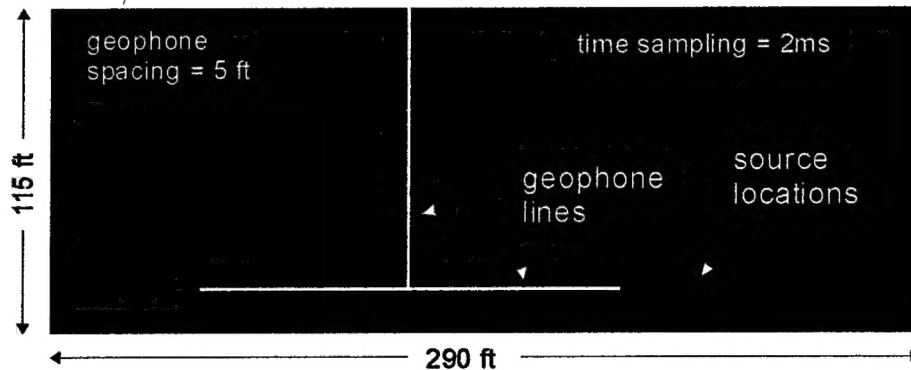
Figure 9. Measurement geometry used for the moving source study.

Figure 10a shows the estimated location (red) for a single source location and Fig. 10b is the results of the time exposure over all data. Here, the **T** pattern of the source locations is clearly reconstructed.
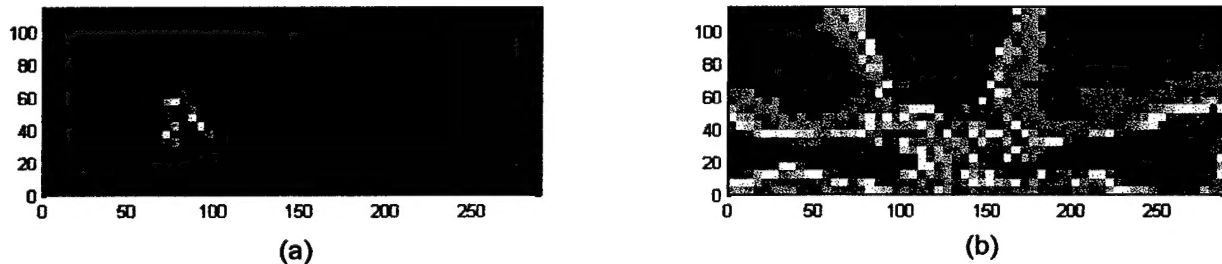
Figure 10. TEA image of (a) a single location and (b) the time exposure image of the moving source.

7. Phase I Summary Conclusions

A Time Exposure Acoustics algorithm has been developed for locating underground noise sources by passive monitoring on the ground surface. This algorithm has been tested on both synthetic data and real data with equally good results. Of particular importance is the discovery that an entire underground void system can be imaged based on noise from a single location. This is a result of the excitation of resonant modes within this subsurface structure.

The computational performance of the algorithm is such that it is possible for it to be used for real time acquisition and processing for detecting and monitoring underground facilities.

8. Plans for Phase II

Phase II, if granted, will included the following works in theory and field tests:

- Refinement of the TEA algorithms – effect of varying acoustic speed in earth, mode conversions, and surface waves (ground rolls); increased image resolution.

- Planned field tests for moving vehicles and other targets:

    1. Open highways – visible ground truths
    2. Highway tunnels – example: I-40 across the Appalachian mountain in the western NC
    3. Underground mines – example: coalmines in the mountain; excavators, loaders, conveyer belts, ore bucket lifts, and occasional blasts.
    4. Known active UGFs – to be coordinated with AFOSR

- Design study for a dedicated TEA hardware and software – DSP level parallel processing for realtime deployment

References

S. J. Norton and I. J. Won, 2000, Time Exposure Acoustics, IEEE Transaction on Geoscience and Remote Sensing, vol. 39, pp. 1337-1343.

A. J. Witten, 1991, The Application of a Maximum Likelihood Estimator to Tunnel Detection, Inverse Problems, vol. 7, pp. L49 – L55.

A. J. Witten, T. E. Levy, J. Ursic, and P. White, 1995, Geophysical Diffraction Tomography: New Views on the Shiqmim Prehistoric Subterranean Village Site (Israel), Geoarchaeology, vol. 10, pp. 97 – 118.

A. J. Witten, A. Schatzberg, and A. J. Devaney, 1995, Vector Radar Diffraction Tomography Maximum Likelihood Estimation, Journal of Environmental and Engineering Geophysics, vol. 0, pp. 91 -104.

A. J. Witten, I. J. Won, and S. J. Norton, 1997, Subsurface Imaging with Broadband Electromagnetic Induction, Inverse Problems, pp. 1621 – 1639.

J. Witten, I. J. Won, and S. J. Norton, 1997, Imaging Underground Structures Using Broadband Electromagnetic Induction, Journal of Environmental and Engineering Geophysics, vol. 2, pp. 105 – 114.

Appendix A: TEA Imaging Algorithm
Appendix B: A reprint: "Time Exposure Acoustics," by S. J. Norton and I. J. Won, Published in 2000 in IEEE Transaction on Geoscience and Remote Sensing, vol. 39, pp. 1337-1343.

Appendix A: TEA Imaging Algorithm

1. Formulation of the Problem

Let $u(\mathbf{r}_n, t)$ denote the signal recorded at the point $\mathbf{r}_n$ on the surface (i.e., $\mathbf{r}_n$ is the position of the n-th geophone) and let c be the velocity of sound (assumed constant). See figure 1.
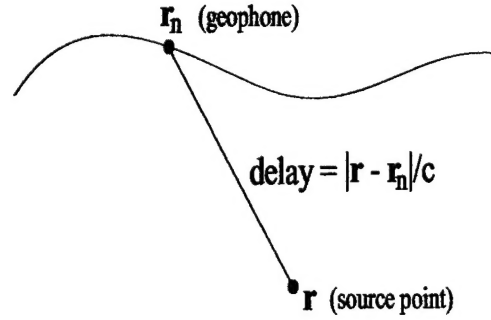
Received signal: $\mathbf{u}(\mathbf{r}_n, t)$

Fig. 1. One source point and one receiver point.

The image, $\mathcal{O}(\mathbf{r})$, is computed by backpropagating the received signals, $u(\mathbf{r}_n, t)$, back to the source point, $\mathbf{r}$, and summing over the geophones. This is described by the formula:

$$\mathcal{O}(\mathbf{r}) = \sum_{n=1}^{N} \hat{u}(\mathbf{r}_n, |\mathbf{r} - \mathbf{r}_n|/c) \, |\mathbf{r} - \mathbf{r}_n|, \tag{1}$$

where $\hat{u}(\mathbf{r}_n, t)$ means a (possibly) filtered version of $u(\mathbf{r}_n, t)$, that is,

$$\hat{u}(\mathbf{r}_n, t) = u(\mathbf{r}_n, t) * F(t), \tag{2}$$

with $*$ denoting convolution and $F(t)$ a filter function. For example, $F(t)$ might be a whitening filter designed to boost the higher frequencies. In (1) the factor $|\mathbf{r} - \mathbf{r}_n|$ is included to compensate for signal loss due to geometric spreading of the wave originating from the point $\mathbf{r}$. This factor is optional and simulations show that its inclusion does not have a very noticeable effect on image quality. Note that in (1), the signal $\hat{u}(\mathbf{r}_n, t)$ is evaluated at the time $t = |\mathbf{r} - \mathbf{r}_n|/c$; this correctly describes backpropagation to the point $\mathbf{r}$ if the time origin ($t = 0$) occurred when the signal

1

was emitted from $\mathbf{r}$. However, the time origin is unknown. This point is discussed further below.

Now, for brevity, define $\hat{u}_n(\mathbf{r}) = \hat{u}(\mathbf{r}_n, |\mathbf{r} - \mathbf{r}_n|/c)|\mathbf{r} - \mathbf{r}_n|$, so that (1) is

$$\mathcal{O}(\mathbf{r}) \; = \; \sum_{n=1}^{N} \hat{u}_n(\mathbf{r}). \tag{3}$$

The function $\hat{u}_n(\mathbf{r})$ is a random variable with zero mean. Letting $E\{\cdot\}$ denote statistical expectation (or ensemble average), we see that $E\{\mathcal{O}(\mathbf{r})\} = 0$ since the image $\mathcal{O}(\mathbf{r})$ is linear in the field $u(\mathbf{r}, t)$. This precludes averaging the images on an "amplitude" basis. We therefore consider averaging successive images on an intensity basis, i.e., averaging $|\mathcal{O}(\mathbf{r})|^2$. This, however, leads to a large "DC bias" in the image that builds up over time. An unbiased image estimator is obtained by subtracting the "DC component," as follows:

$$\bar{\mathcal{O}}(\mathbf{r}) \; = \; E\left\{ \left| \sum_{n=1}^{N} \hat{u}_n(\mathbf{r}) \right|^2 \right\} \; - \; E\left\{ \sum_{n=1}^{N} |\hat{u}_n(\mathbf{r})|^2 \right\}, \tag{4}$$

which can also be written

$$\bar{\mathcal{O}}(\mathbf{r}) \; = \; \sum_{\substack{n=1 \\ n \neq m}}^{N} \sum_{m=1}^{N} E\{\hat{u}_n(\mathbf{r})\hat{u}_m(\mathbf{r})^*\}, \tag{5}$$

where $*$ means complex conjugate. For generality, we allow the fields $u_n(\mathbf{r})$ to be complex, because we may choose $u(\mathbf{r}, t)$ to represent either a real quantity or its analytic signal, which is complex. Equation (5) shows that, if there is no correlation between distinct traces, $\hat{u}_n(\mathbf{r})$, then the image $\bar{\mathcal{O}}(\mathbf{r})$ vanishes as desired. The first term in (4) bears some resemblance to the coherence measure called the semblance [1].

Suppose we denote by $\mathcal{O}^{(k)}(\mathbf{r})$ the k-th image realization. We wish to average many such realizations to approximate the ensemble average indicated by the expectation operator $E\{\cdot\}$ in (4). The index k may be thought of as a time index. At each time increment, we compute a complete image, which requires a summation over all geophones for each pixel in the image. We can average these images recursively, as follows. The average of M images is

$$\bar{\mathcal{O}}_M(\mathbf{r}) \; = \; \frac{1}{M} \sum_{k=1}^{M} \mathcal{O}^{(k)}(\mathbf{r}), \tag{6}$$

where the k-th realization is defined by

$$\mathcal{O}^{(k)}(\mathbf{r}) \; = \; \left| \sum_{n=1}^{N} \hat{u}_n^{(k)}(\mathbf{r}) \right|^2 \; - \; \sum_{n=1}^{N} |\hat{u}_n^{(k)}(\mathbf{r})|^2. \tag{7}$$

2

One can update the average (6) recursively as more data become available. That is, given the average formed after M image realizations, i.e., $\bar{\mathcal{O}}_M(\mathbf{r})$, then the updated mean after the $M+1$ realization, $\mathcal{O}^{(M+1)}(\mathbf{r})$, becomes available is

$$\bar{\mathcal{O}}_{M+1}(\mathbf{r}) = \frac{M}{M+1}\bar{\mathcal{O}}_M(\mathbf{r}) + \frac{1}{M+1}\mathcal{O}^{(M+1)}(\mathbf{r}). \tag{8}$$

In practice, it may be easier to record a finite record of data, say, of K samples, and then reconstruct K images and simply average these, rather than to use the above recursive algorithm at every time increment. The recursive procedure could then be used on the sets of averaged K images. If K is not too large, the latter approach shouldn't require storage of an unmanageable amount of data. We can write this averaging process with respect to k more explicitly as follows. To average K images at K times t_k, we can write the first term in (4) as follows:

$$\mathcal{O}_1^{(k)}(\mathbf{r}) = \frac{1}{K}\sum_{k=1}^{K}\left|\sum_{n=1}^{N}\hat{u}(\mathbf{r}_n, t_k + |\mathbf{r} - \mathbf{r}_n|/c)\,|\mathbf{r} - \mathbf{r}_n|\right|^2 \tag{9}$$

and the second term in (4) as

$$\mathcal{O}_2^{(k)}(\mathbf{r}) = \frac{1}{K}\sum_{k=1}^{K}\sum_{n=1}^{N}|\hat{u}(\mathbf{r}_n, t_k + |\mathbf{r} - \mathbf{r}_n|/c)|^2\,|\mathbf{r} - \mathbf{r}_n|^2. \tag{10}$$

Essentially, we are reconstructing images (via coherent summation over all geophones in (9)) at all time origins, t_k.

2. Programming Considerations

To describe the algorithm, let N_{pixels} be the number of pixels, N_{geo} the number of geophones, and N_K the number of time samples in the current data record. Let $R(N_{pixels}, N_{geo})$ denote an array dimensioned as indicated that contains the pre-computed distances between each pixel and each geophone. Let the data array be given by $Data(N_K, N_{geo})$ and let $Image(N_{pixels})$ denote an array that stores the image. The latter array is initialized to zero before starting the algorithm. Let c be the velocity of sound and let dt denote the sampling interval. The algorithm then reads as follows.

```
1          do k=N_K
2            do i=N_pixels
3              sum_1 = 0
4              sum_2 = 0
5
6              do j=1,N_geo
7                delay = R(i,j)/c
8                ik = round(delay/dt + k)
9                sum_1 = sum_1 + Data(ik,j)
10               sum_2 = sum_2 + Data(ik,j)**2
11             end
12
13             image(i) = image(i) + sum_1**2 - sum_2
14           end
15         end
```

Line 7 computes the propagation delay between the j-th geophone and the i-th pixel. Line 8 rounds this to an integer index that is used to select the time index ik in the data array Data(ik,j). Note that the incoherent average is performed with respect to the index k (time) and the coherent average is performed with respect to the index j (geophone).

3. Caveats

This algorithm is very simple. It continually backpropagates as new data arrive and sums the images on an intensity basis. As described, the algorithm neglects variations in the sound velocity, assumes one type of (scalar) wave, assumes perfect knowledge of the geophone coordinates, and assumes that the sources are broadband and spatially incoherent (uncorrelated). Also, the geophone spacing is assumed small enough so that spatial frequency aliasing is not a problem at the higher frequencies. Departures from any of these assumptions will of course tend to degrade image quality.

Reference

1. N. S. Neidell and M. T. Taner, Semblance and other coherency measures for multichannel data, Geophysics **36**, 482-497 (1971).

Time Exposure Acoustics

Stephen J. Norton and I. J. Won

Abstract—An analysis of a passive seismic method for subsurface imaging is presented, in which ambient seismic noise is employed as the source of illumination of underground scatterers. The imaging algorithm can incorporate new data into the image in a recursive fashion, which causes image background noise to diminish over time. Under the assumption of spatially-incoherent ambient noise, an analytical expression for the point-spread function of the imaging algorithm is derived. The point-spread function (PDF) characterizes the resolution of the image, which is a function of the receiving array length and the ambient noise bandwidth. Results of a Monte Carlo simulation are presented to illustrate the theory.

Index Terms—Acoustic imaging, acoustic tomography, geophysical inverse problems, geophysical signal processing, geophysical tomography, image reconstruction, seismic inverse problems.

I. INTRODUCTION

IN time-exposure photography, low intensity light is integrated over time to enhance image brightness. A similar concept is applicable in acoustics, wherein acoustic or seismic imaging is performed using ambient acoustic noise as a constant source of "illumination." The idea of passive acoustic imaging was recently demonstrated in an ocean environment by Buckingham and collaborators, in which submerged scatterers were imaged using ambient acoustic noise generated by surface wave action [1]–[3]. The authors refer to this method as "acoustic daylight imaging." We propose extending the concept to seismic imaging of subsurface scatterers, including natural and manmade underground structures. Sources of ambient seismic noise are microseisms and surface noise due to weather and human activity.

Ambient imaging is potentially attractive since it avoids the high cost of the deployment and operation of active seismic sources. Moreover, ambient illumination is everpresent, thus permitting the "integration" of ambient data over an extended time period. In this way, relatively weak scatterers should eventually reveal themselves after a sufficient accumulation of data.

The basis of an imaging method using ambient illumination can be explained as follows. Seismic or acoustic waves impinging on a scatterer will create a scattered wavefront that will manifest itself as a spatially correlated signal over a receiving array on the surface. By coherently summing this correlated signal using a suitable migration (or backpropagation) procedure, the image of a weak scatterer should grow stronger over time relative to the uncorrelated background noise. One can conceive of devising an imaging algorithm that develops an image of the target as new data are incorporated into the image in a

recursive manner. In this way, storage of large quantities of data prior to forming the image can be avoided.

In the seismic domain, a few previous attempts have been reported on passively detecting large reflecting structures (e.g., a bedrock interface) [4]–[7]. As far as we are aware, however, no attempts have been made to image scatterers or diffracting structures (i.e., structures comparable to the wavelength of the illuminating waves) using ambient illumination. A more complete review of published work on passive seismic methods can be found in a recent report from the Oak Ridge National Laboratory, Oak Ridge, TN, [8] that presents results of a preliminary study on the feasibility of subsurface ambient imaging. In that study, no imaging was attempted using real data, but some important facts were established. First, ambient noise in the appropriate frequency range (up to 100 to 200 Hz) has adequate energy to be used for subsurface imaging, and second, cross-correlation of noise recorded by geophones in a two-dimensional (2-D) array showed peaks that relate to seismic energy propagating across the array. It was determined that the source of this spatially-coherent energy was traffic from a nearby road. An implication of the report is that the ability to suppress surface wave energy by digital filtering or optimal array design is critically important in separating ground roll from the upward propagating body waves scattered from subsurface structures.

An essential difference between active and ambient illumination is that, in the latter case, no time origin exists with respect to which propagation delays can be referenced. The illumination is effectively continuous and random. A greatly simplified analysis is possible if the illuminating waves can be regarded as spatially incoherent. Spatial incoherence is an idealization implying that the wave fields scattered from two distinct points in space are statistically uncorrelated over time. If waves are arriving from one direction from a distant and localized source, the assumption of spatially-incoherent illumination will break down. However, if the source of noise is primarily from the surface, which is generally the case at higher frequencies, then the assumption of spatial incoherence is probably quite good when the averaging is performed over an extended time period. It can be shown that the spatial resolution in an image derived from ambient noise is determined essentially by two factors: the length of the geophone array and the spatial coherence length of the noise. The latter is approximately the speed of sound divided by the noise bandwidth. For analytical tractability, we assume scatterers embedded in a background of constant velocity. Although the uniform background assumption is somewhat artificial, our primary aim in this paper is to investigate the resolution limits of a passive imaging scheme and relate it to the statistical properties of the seismic noise.

Below, an expression for the point-spread function (PSF, which is the image of a point scatterer) of an ambient imaging

system is derived assuming complete spatial incoherence of the noise. Suppose that $p(\mathbf{r}_1 : t_1)$ and $p(\mathbf{r}_2 : t_2)$ are signals scattered from the point $\mathbf{r}_1$, and $\mathbf{r}_2$. Then, complete spatial incoherence can be expressed as

$$E[p(\mathbf{r}_1 : t_1) \, p(\mathbf{r}_2 : t_2)^*] = P(t_1 - t_2) \, \delta(\mathbf{r}_1 - \mathbf{r}_2) \qquad (1)$$

where $E[\cdot]$ denotes statistical expectation (i.e., an ensemble average), $\delta(\mathbf{r}_1 - \mathbf{r}_2)$ is a three-dimensional (3-D) Dirac delta function, and $P(\tau)$ is the temporal autocorrelation function of the noise. Here, we assume a stationary random process, implying that the argument of $P(\tau)$ is a function of the time difference $\tau = t_1 - t_2$. In (1), * denotes complex conjugate, since we reserve the option of working with analytic signals. We should point out that the relation (1) makes sense for a spatially incoherent source, but for a scattering problem, (1) will always represent an approximation whenever the autocorrelation function $P(\tau)$ has some finite duration (i.e., when the noise is bandlimited). This is because an incident waveform that is correlated over a finite time (given by the reciprocal of its bandwidth) will give rise to scattering that is spatially correlated over distances up to the spatial correlation length of the noise, given by c/B, where B is the bandwidth of the noise, and c is the speed of sound. As a consequence, the Dirac delta function in (1) will be broadened by this amount. If we consider scatterers farther apart than c/B, then the relation (1) effectively holds. In an imaging algorithm, it thus makes sense to make our pixel size larger than this correlation length. Image resolution can also be improved to some extent by applying a prewhitening filter to the received signals prior to image formation. Such a filter can help flatten the spectral response over the available bandwidth which, in the spatial domain, translates into a narrow point response.

The assumption of complete incoherence, expressed by (1), considerably simplifies the derivation of an analytical expression for the PSF. Later, we compare the analytically derived PSF to a more realistic computation of the PSF based on a Monte Carlo simulation of bandlimited stochastic noise using a random number generator. We shall see that the Monte Carlo simulation shows good agreement with the analytically derived PSF. The simulated images of several scatterers were obtained for various numbers of exposures, where each "exposure" refers to one image realization generated from one set of independent data. "Independent data" means that the interval of time separating data sets is taken to be greater than the reciprocal of the bandwidth of the noise. Assuming a bandwidth extending to 200 Hz, this implies an exposure interval of 0.005 s. Thus, 100 000 exposures would take no shorter than about 500 seconds of recording time. We will see that, as the number of exposures that are averaged increases, a gradual reduction in the uncorrelated background noise in the image is evident as data are continuously incorporated.

In the analysis that follows, we make several idealizing assumptions for the sake of analytical tractability, such as the assumption that stochastic scattering can be modeled as a weighted superposition of incoherent sources, and that multiple scattering is sufficiently small to neglect. It is likely, however, that the success of the method will not rest crucially on any of these idealizations, although performance may depart
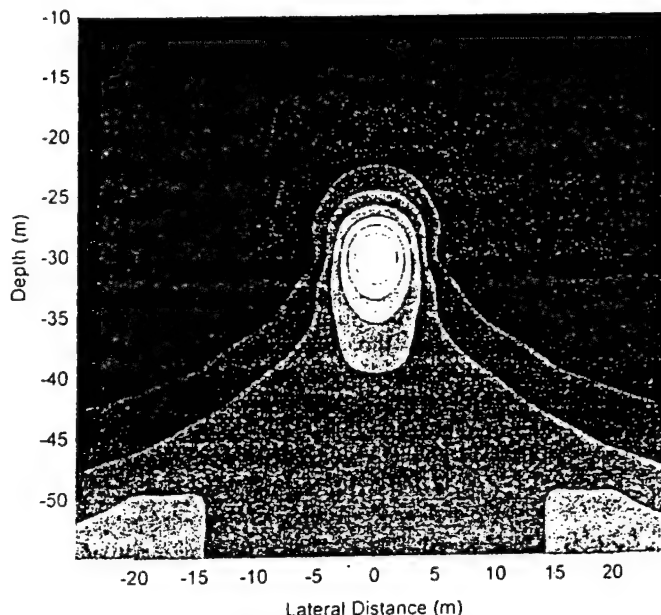

Fig. 1. Point-spread function (PSF) for a scatterer at a depth of 30 m, computed using (16) with surface data only.

somewhat from the results predicted by the analysis based on our simplifying assumptions.

II. IMAGING ALGORITHM

We model the earth as a distribution of scatterers of varying strengths (scattering cross-sections) embedded in a uniform background of constant velocity c. The extension to the case of nonuniform velocity can be made, provided that velocity information can be derived by independent means. We assume that the scattering medium is illuminated with broadband, spatially-incoherent noise. The noise is then passively recorded on the surface of the earth at N measurement points over some interval of time. Our objective is to reconstruct, or image, the scattering density distribution by backpropagating (migrating) the recorded noise into the earth. Because the source of illumination is always "turned on," an image of the scattering distribution can be gradually improved over time by recursively incorporating new data. The imaging algorithm coherently sums over the wavefront scattered from a point in the earth (equivalent to coherently summing along a hyperbolic path in the space-time domain) and assigns this value to the corresponding image point. This process is repeated for all image points until an entire image is generated. Multiple images created over successive time intervals are then added on an intensity basis as described below. As more data are incorporated, simulations show that the stochastic variability in the (mean) image due to the random nature of the illumination gradually diminishes, and weak scattering features become more apparent. After a certain large number of iterations, the image ceases to improve since all image noise has effectively been averaged out. Any remaining artifacts (e.g., the finite PSF width and sidelobe structure) are due to the inherent resolution limits of the system imposed by finite aperture and bandwidth constraints.
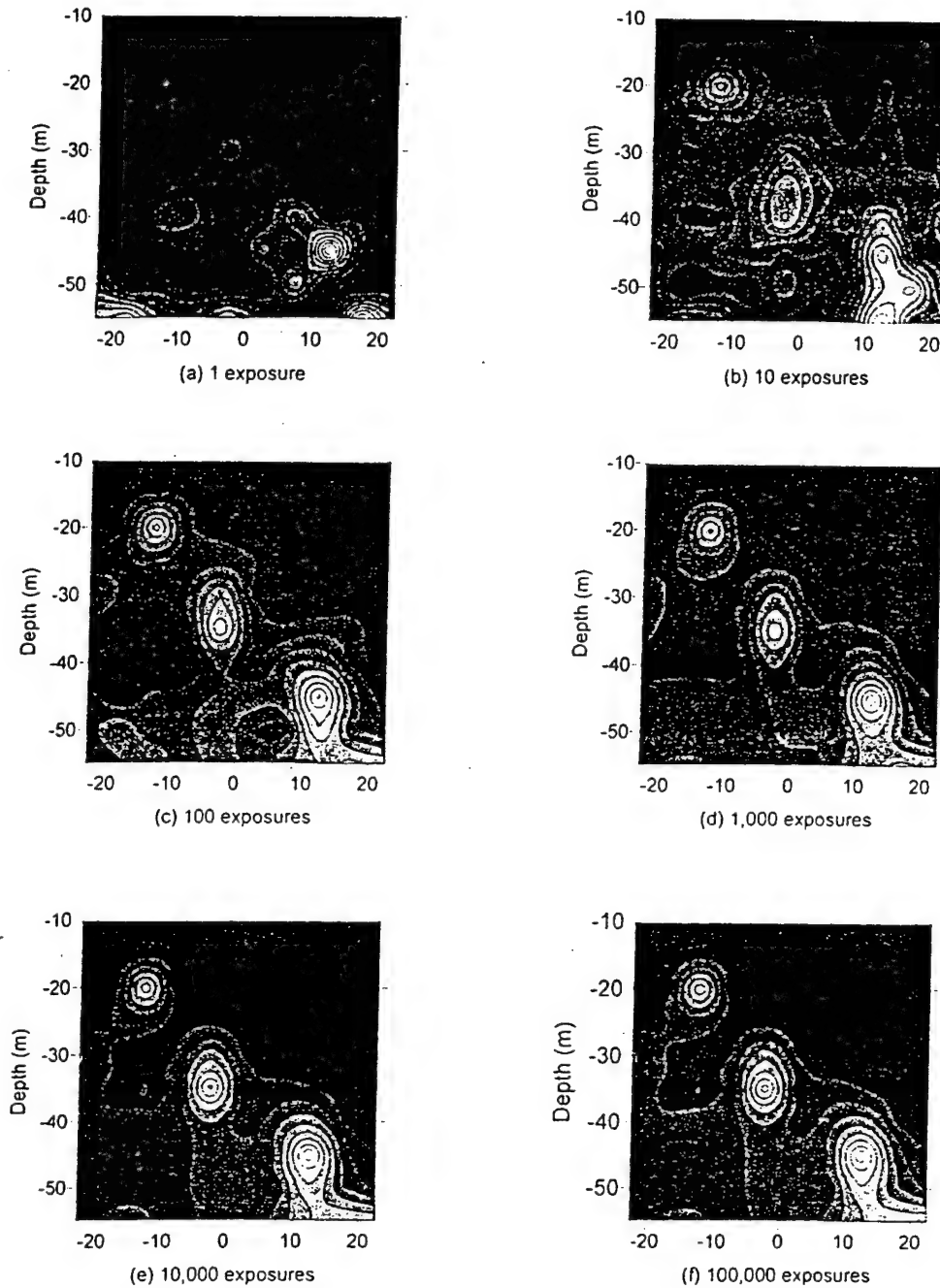
Fig. 2. Normalized images of three scatterers using stochastic data for different numbers of exposures with surface data only.

Below, we describe the imaging algorithm and derive from it the PSF of the system, which may be defined as the image of a single point scatterer. The PSF characterizes the lateral and depth resolution of the imaging system.

Let $u(\mathbf{r}_n, t)$ denote the field recorded at the point $\mathbf{r}_n$ on the Earth's surface. Then the image generated by the process of backpropagation is given by

$$\mathcal{O}(\mathbf{r}) = 4\pi \sum_{n=1}^{N} \hat{u}(\mathbf{r}_n, |\mathbf{r} - \mathbf{r}_n|/c) |\mathbf{r} - \mathbf{r}_n| \qquad (2)$$

where $\hat{u}(\mathbf{r}_n, t)$ is a filtered version of $u(\mathbf{r}_n, t)$. That is

$$\hat{u}(\mathbf{r}_n, t) = u(\mathbf{r}_n, t) * F(t) \qquad (3)$$

with $*$ denoting convolution and $F(t)$ a specified filter function. For example, $F(t)$ could be a whitening filter. In (2), the factor $4\pi |\mathbf{r} - \mathbf{r}_n|$ is included to compensate for signal loss due to geometric spreading of the wave originating from the point $\mathbf{r}$.

For brevity, define $\hat{u}_n(\mathbf{r}) = 4\pi \hat{u}(\mathbf{r}_n, |\mathbf{r} - \mathbf{r}_n|/c) |\mathbf{r} - \mathbf{r}_n|$ so that (2) may be written

$$\mathcal{O}(\mathbf{r}) = \sum_{n=1}^{N} \hat{u}_n(\mathbf{r}). \qquad (4)$$

The noise field $\hat{u}_n(\mathbf{r})$ is a random variable with zero mean. Letting $E\{\cdot\}$ denote statistical expectation (or ensemble average), we see that $E\{\mathcal{O}(\mathbf{r})\} = 0$, since the image $\mathcal{O}(\mathbf{r})$ is linear in the field $u(\mathbf{r}, t)$. This precludes averaging the images on an "amplitude" basis. We therefore consider averaging successive images on an intensity basis (i.e., averaging $|\mathcal{O}(\mathbf{r})|^2$). This, however, leads to a large DC bias in the image that builds up over time. An unbiased image estimator is obtained by subtracting the DC component as follows:

$$\overline{\mathcal{O}}(\mathbf{r}) = E\left\{\left|\sum_{n=1}^{N}\hat{u}_n(\mathbf{r})\right|^2\right\} - E\left\{\sum_{n=1}^{N}|\hat{u}_n(\mathbf{r})|^2\right\} \quad (5)$$

which can also be written

$$\overline{\mathcal{O}}(\mathbf{r}) = \sum_{\substack{n=1 \\ n \neq m}}^{N}\sum_{m=1}^{N} E\{\hat{u}_n(\mathbf{r})\hat{u}(\mathbf{r})^*\}. \quad (6)$$

Equation (6) shows that if there is no correlation between distinct traces $\hat{u}_n(\mathbf{r})$, then the image $\overline{\mathcal{O}}(\mathbf{r})$ vanishes as desired. Otherwise, it is positive. The first term in (5) bears some resemblance to the coherence measure called the semblance [9].

Suppose we denote by $\mathcal{O}^{(k)}(\mathbf{r})$ the kth image realization. We wish to average many such realizations to approximate the ensemble average indicated by the expectation operator $E\{\cdot\}$ in (5). That is, the average of M images is

$$\overline{\mathcal{O}}_M(\mathbf{r}) = \frac{1}{M}\sum_{k=1}^{M}\mathcal{O}^{(k)}(\mathbf{r}) \quad (7)$$

where the kth realization is defined by

$$\mathcal{O}^{(k)}(\mathbf{r}) = \left|\sum_{n=1}^{N}\hat{u}_n^{(k)}(\mathbf{r})\right|^2 - \sum_{n=1}^{N}|\hat{u}_n^{(k)}(\mathbf{r})|^2. \quad (8)$$

To avoid storing large amounts of data, one can update the average (7) recursively as more data become available. Given the average $\overline{\mathcal{O}}_M(\mathbf{r})$ formed after M image realizations, the updated average $\overline{\mathcal{O}}_{M+1}(\mathbf{r})$ after the $M + 1$ realization $\mathcal{O}^{(M+1)}(\mathbf{r})$ becomes available is

$$\overline{\mathcal{O}}_{M+1}(\mathbf{r}) = \frac{M}{M+1}\overline{\mathcal{O}}_M(\mathbf{r}) + \frac{1}{M+1}\mathcal{O}^{(M+1)}(\mathbf{r}). \quad (9)$$

III. DERIVATION OF SYSTEM POINT SPREAD FUNCTION

Below, we derive an analytical form for the PSF. Our basic objective is to evaluate analytically the first term in (5), which represents the actual image. The purpose of the second term is essentially to eliminate a DC bias, or constant background, from this image. For analytical tractability, we assume that the receiving array is continuously sampled, in which case the sum over n in (5) becomes an integral over the array aperture. We model the medium as a continuum of scatterers embedded in a background of constant velocity c. The density of scatterers at the point $\mathbf{r}$ is denoted by $\sigma(\mathbf{r})$. That is, $\sigma(\mathbf{r})$ can be regarded as a continuously varying scattering cross-section, and our objective
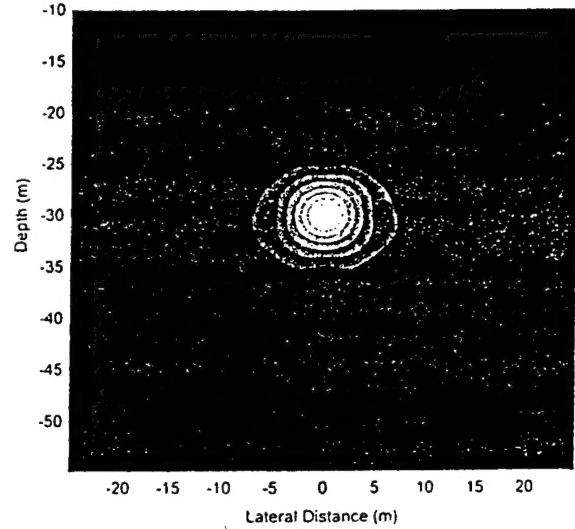

Fig. 3. PSF for a scatterer computed using (16). assuming both surface and borehole data.

is to reconstruct $\sigma(\mathbf{r})$. Suppose random noise is illuminating the medium from many directions, and let $p(\mathbf{r}; t)$ denote the noise scattered from the point $\mathbf{r}$. Then the signal received at a point $\mathbf{r}_a$ on the array may be written as the following integral over the medium

$$u(\mathbf{r}_a, t) = \iiint \sigma(\mathbf{r}')\frac{p[\mathbf{r}'; t - |\mathbf{r}' - \mathbf{r}_a|/c]}{4\pi|\mathbf{r}' - \mathbf{r}_a|}d^3\mathbf{r}'. \quad (10)$$

In this simple model, multiple scattering has been neglected. For a 3-D reconstruction, we record data over a 2-D array on the surface of the earth. Letting $\mathbf{r}_a$ represent a point on this array and A the region of the surface occupied by the array, then the backpropagation operation can be expressed as follows, where, for generality, we again allow filtering prior to backpropagation:

$$\mathcal{O}(\mathbf{r}) = 4\pi \iint_A d^2\mathbf{r}_a\,\hat{u}(\mathbf{r}_a, |\mathbf{r} - \mathbf{r}_a|/c)\,|\mathbf{r} - \mathbf{r}_a| \quad (11)$$

which is the continuous space analogue of (2). Once again, $\hat{u}(\mathbf{r}_a, t)$ is a filtered version of the recorded data $u(\mathbf{r}_a, t)$, i.e.,

$$\hat{u}(\mathbf{r}_a, t) = u(\mathbf{r}_a, t) * F(t) \quad (12)$$

for a specified filter function $F(t)$.

To compute the image, we substitute (10) into (11) and interchange orders of integration. This gives

$$\mathcal{O}(\mathbf{r}) = \iiint d^3\mathbf{r}'\,\sigma(\mathbf{r}')\iint_A d^2\mathbf{r}_a$$
$$\cdot\frac{|\mathbf{r} - \mathbf{r}_a|}{|\mathbf{r}' - \mathbf{r}_a|}\hat{p}[\mathbf{r}'; |\mathbf{r} - \mathbf{r}_a|/c - |\mathbf{r}' - \mathbf{r}_a|/c] \quad (13)$$

where $\hat{p}(\mathbf{r}; t) = p(\mathbf{r}; t) * F(t)$. Now take the absolute square of (13), perform an ensemble average, and use the relation (1). This gives rise to the following result:

$$E[|\mathcal{O}(\mathbf{r})|^2] = \iiint d^3\mathbf{r}'\,\sigma(\mathbf{r}')^2\,\mathrm{PSF}(\mathbf{r}; \mathbf{r}') \quad (14)$$
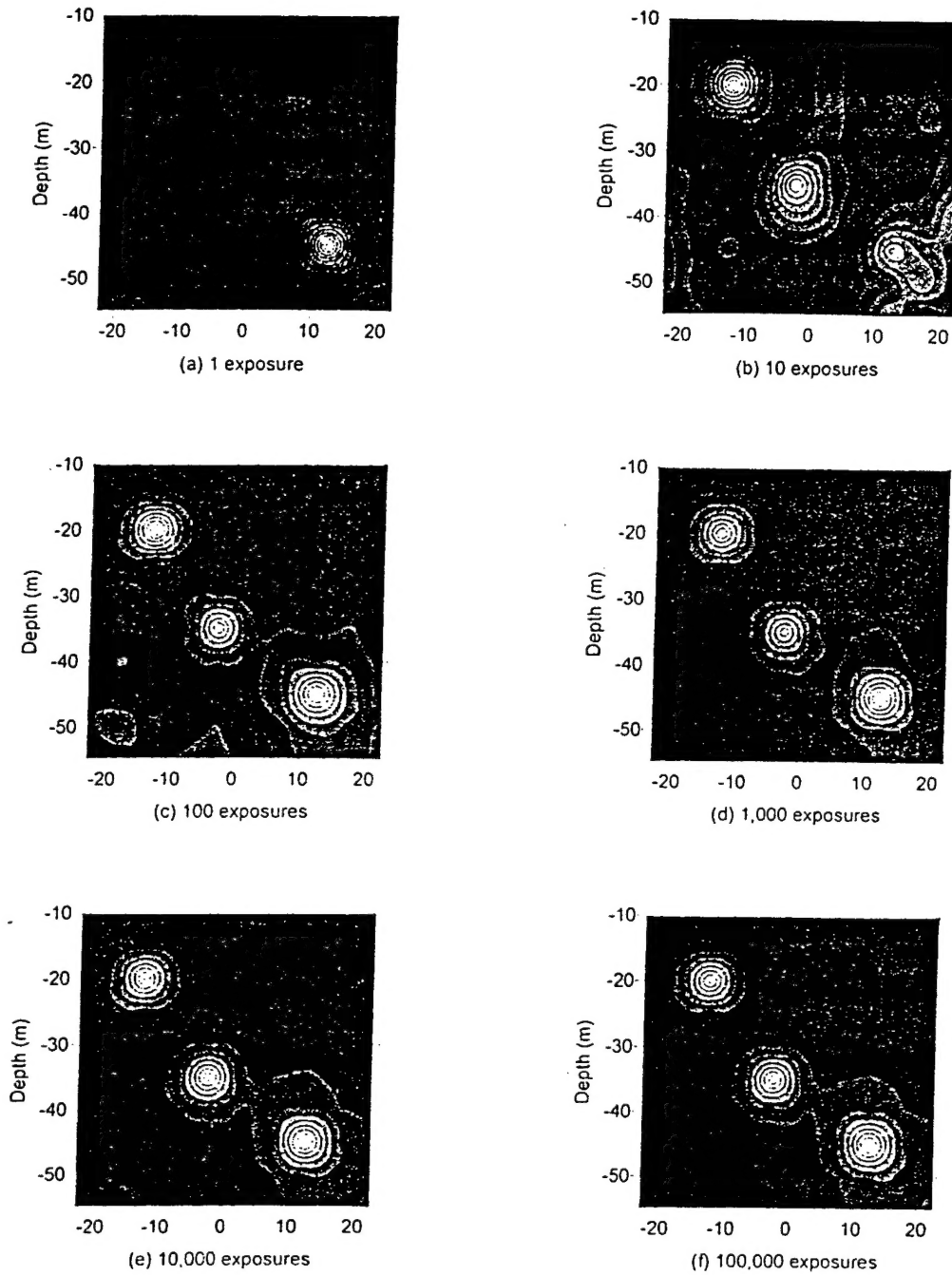
Fig. 4. Normalized images of three scatterers using stochastic data for different numbers of exposures assuming both surface and borehole data.

where PSF$(\mathbf{r}; \mathbf{r}')$ is the PSF defined by

$$\text{PSF}(\mathbf{r}; \mathbf{r}') \equiv \iint\limits_{A} d^2\mathbf{r}_a \frac{|\mathbf{r} - \mathbf{r}_a|}{|\mathbf{r}' - \mathbf{r}_a|} \iint\limits_{A} d^2\mathbf{r}'_a$$

$$\cdot \frac{|\mathbf{r} - \mathbf{r}'_a|}{|\mathbf{r}' - \mathbf{r}'_a|} \hat{P}[(R_a - R'_a)/c] \qquad (15)$$

with

$$R_a \equiv |\mathbf{r} - \mathbf{r}_a| - |\mathbf{r}' - \mathbf{r}_a|$$
$$R'_a \equiv |\mathbf{r} - \mathbf{r}'_a| - |\mathbf{r}' - \mathbf{r}'_a|.$$

In (15), $\hat{P}(\tau)$ is the filtered version of $P(\tau)$, i.e., $\hat{P}(\tau)$ is the autocorrelation function $E[\hat{p}(\mathbf{r}; t + \tau)\hat{p}^*(\mathbf{r}; t)]$.

We can simplify the above expression for the PSF as follows. Let $\tilde{P}(\omega)$ denote the Fourier transform of $P(t)$, that is

$$P(t) = \int_{-\infty}^{\infty} \tilde{P}(\omega) e^{i\omega t} d\omega.$$

Note that $\tilde{P}(\omega)$ is the noise power spectrum. Then

$$\tilde{P}(t) = \int_{-\infty}^{\infty} \tilde{P}(\omega) |\tilde{F}(\omega)|^2 e^{i\omega t} d\omega$$

where $\tilde{F}(\omega)$ is the Fourier transform of the filter function $F(t)$. Substituting this into (15) results in

$$\text{PSF}(\mathbf{r}; \mathbf{r}') = \int_{-\infty}^{\infty} d\omega \, \tilde{P}(\omega) |\tilde{F}(\omega)|^2 |A_\omega(\mathbf{r}; \mathbf{r}')|^2 \qquad (16)$$

where

$$A_\omega(\mathbf{r}; \mathbf{r}') \equiv \iint_A d^2 \mathbf{r}_a \frac{|\mathbf{r} - \mathbf{r}_a|}{|\mathbf{r}' - \mathbf{r}_a|}$$
$$\cdot \exp[i\omega(|\mathbf{r} - \mathbf{r}_a| - |\mathbf{r}' - \mathbf{r}_a|)/c]. \qquad (17)$$

Clearly, at each frequency ω, the function $A_\omega(\mathbf{r}; \mathbf{r}')$ will become large when the image point r coincides with the scattering point $\mathbf{r}'$ since then the exponent vanishes. In the next section, we show a numerical computation of the PSF using (16) and (17), and compare it to a Monte Carlo simulation.

IV. SIMULATIONS

Fig. 1 shows an image of PSF $\text{PSF}(\mathbf{r}; \mathbf{r}_0)$ obtained by numerically evaluating (16) and (17) over a linear array. In computing the PSF, the scattering point was placed at $\mathbf{r}' = (0, -30)$ in units of meters. Twenty receiving elements were assumed, spaced at 5-m intervals (implying an array length of 95 m). The power spectrum $\tilde{P}(\omega)$ was assumed, for simplicity, to extend uniformly to 200 Hz. A velocity of sound of 500 m/s was used. We note that if the velocity is scaled up and the noise bandwidth remains unchanged then the appearance of all images will remain unchanged, provided all distances are scaled in proportion to the velocity.

Fig. 2 shows the results of a Monte Carlo simulation using (7) and (8), which combine multiple image realizations, each generated by the backpropagation process defined by (2). In the simulation, three scatterers were assumed at coordinates $(-12.5, -20)$, $(-2.5, -35)$, and $(12.5, -45)$. We regarded each of these three points as behaving effectively as independent sources of broadband random noise. As noted, this is a reasonable model when the noise correlation distance is smaller than the scatterer separations. Finally, surface interactions and multiple scattering between the scatterers were neglected in the simulation.

The number of exposures indicated in Fig. 2 is defined as the number of terms M in the summation (7). In each image realization, backpropagation to a 10×10 array of pixels was performed with a center-to-center pixel separation of 5 m. The simulated scattered waveform $u(\mathbf{r}, t)$ was created using a random number generator to produce a zero-mean, uniformly distributed sequence of samples at a sampling interval of 0.0025 s, corresponding to a Nyquist rate of 200 Hz. This implies a noise correlation length c/B equal to 2.5 m when $B = 200$ Hz and $c = 500$ m/s. Thus, the center-to-center pixel spacing is greater than the correlation length. The numbers of exposures averaged are indicated in the figure. Each image has been normalized to unity to show clearly how background artifacts are reduced as the exposure number increases. In this particular simulation, the image

quality reaches a steady state above about 1000 exposures. This means that nearly all of the stochastic variability has been eliminated at this point, and the remaining artifacts (PSF broadening and sidelobe structure) are determined by the inherent bandwidth and aperture limitations of the system.

The above simulation assumed an array of 20 geophones on the surface of the earth. Another simulation was performed with both surface geophones and borehole geophones. The same scatterers, velocity, and noise bandwidth were assumed. In this case, however, 60 geophones were assumed in the simulation, 20 on the surface, 20 distributed vertically down a borehole to the left of the scattering region, and 20 in a borehole to the right of the scattering region. The three geophone array segments, one surface and two borehole, were assumed to be of the same length (95 m). The PSF for this array configuration was again computed using (16) and (17) and is shown in Fig. 3. Next, the results of a Monte Carlo simulation are shown in Fig. 4. Note that both the PSF and the simulated images are sharper and more symmetrical due to the extended system aperture created by the addition of the boreholes data.

V. CONCLUSION

A theoretical investigation of the possibility of imaging underground scatterers employing ambient illumination was presented. For simplicity, we assumed that the scatterers were embedded in a constant velocity background, but the extension to nonuniform velocity is expected to yield qualitatively similar results. Under the assumption of spatially incoherent noise, an analytical expression for the PSF was derived. This expression characterizes both transverse and depth resolution and defines their dependence on array length and the ambient noise bandwidth. Monte Carlo simulations were performed to demonstrate that multiple exposures, added together as data are continuously acquired, will diminish uncorrelated background noise and improve image quality.

REFERENCES

[1] M. J. Buckingham, B. V. Berkhout, and S. A. Glegg, "Imaging the ocean with ambient noise," *Nature*, vol. 356, pp. 327–329, 1992.
[2] M. J. Buckingham, "Theory of acoustic imaging in the ocean with ambient noise," *J. Comut. Acoust.*, vol. 1, pp. 117–140, 1993.
[3] J. R. Potter, "Acoustic imaging using ambient noise: Some theory and simulation results," *J. Acoust. Soc. Amer.*, vol. 95, pp. 21–33, 1994.
[4] L. J. Katz, "Microtremor analysis of local geologic conditions," *Bull. Seis. Soc. Amer.*, vol. 66, pp. 45–60, 1985.
[5] ———, "Passive seismic groundnoise: A novel approach to exploration, Extended abstract," in *Proc. 55th Annu. Int. Meeting Society Exploration Geophysicists*, Washington, DC, 1989, pp. 181–183.
[6] S. P. Cole, "Passive seismic and drill-bit experiments using 2-D arrays," Ph.D. thesis, Stanford University, Stanford, CA, 1996.
[7] S. P. Cole, J. F. Claerbout, D. E. Nichols, and L. Zhang, , "The ambient siesmic field in three dimensions," submitted for publication.
[8] W. E. Doll, S. J. Norton, L. J. Gray, and M. D. Morris, "Passive seismic imaging of scatterers," Oak Ridge National Lab., Oak Ridge, TN, Tech. Rep. K/NSP-585, Oct. 1997.
[9] N. S. Neidell and M. T. Taner, "Semblance and other coherency measures for multichannel data," *Geophys.*, vol. 36, pp. 482–497, 1971.
[10] J. W. Goodman, *Fourier Optics*. New York: McGraw-Hill, 1968.

Stephen J. Norton received the B.A. in physics from the University of California, Berkeley, in 1971, and the Ph.D. in applied physics from Stanford University, Stanford, CA, in 1976.

He was a National Research Council (NRC) Postdoctoral Fellow with the National Bureau of Standards from 1977 to 1979, and worked in the fields of medical imaging and the nondestructive evaluation of materials at the National Institute of Standards and Technology, Gaithersburg, MD, from 1979 to 1993. He then spent five years at the Oak Ridge National Laboratory working in the area of geophysical imaging before joining Geophex, Ltd., Raleigh, NC, in 1998. He has published about 75 papers on all aspects of inversion and imaging, including diffraction tomography, magnetic resonance imaging, Mossbauer tomography, ultrasonic imaging in medicine and NDE, Compton scattering tomography, and electromagnetic induction imaging.

I. J. Won received the B.S. degree in mining and petroleum engineering in 1967 from Seoul National University, Seoul, Korea, and the M.S. and Ph.D. degrees in geophysics from Columbia University, New York, in 1971 and 1973, respectively.

He is currently Technical Director and President of Geophex, Ltd., an independent geological and environmental consulting firm based in Raleigh, NC, which he founded in 1983. From 1976 until 1989, he was an Assistant Professor, Associate Professor, and Professor of Geophysics with North Carolina State University, Raleigh. He has published over 70 research and review articles in refereed technical journals and books. He specializes in geophysical applications to geotechnical and environmental problems.